Archive of Applied Mechanics 66 (1996) 326–335 © Springer-Verlag 1996

The influence of elastic waves on dynamic stress intensity factors (two-dimensional problems)

P. H. Wen, M. H. Aliabadi, D. P. Rooke

Summary In this paper, an indirect boundary integral equation method for the solution of dynamic crack problems is presented. The Laplace transform method is used to derive the fundamental solutions for the opening mode (mode I) and the sliding mode (mode II) displacement discontinuity. Accurate dynamic stress intensity factors $K_N(t)$ $(N = I, II)$ resulting from different time-dependent loads on the crack surface are obtained. The specific influences of the various elastic waves on the stress intensity factors can be clearly seen from the results.

Key words dynamic stress intensity, boundary integral equation, indirect BEM, Laplace transform, elastic waves

1 Introduction

The analysis of crack growth preceding the fracture of structures subjected to impact loads requires the knowledge of the dynamic stress intensity factors (DSIF) and their dependence on time, which is influenced by the variation in the stress waves [1]. Numerical methods are usually the only tools available for the evaluation of the DSIF. One of the earliest applications of a numerical method to the solution of a dynamic crack problem was the use of a finite difference method in [2]. Later, the finite element method and the boundary element method were applied successfully to the evaluation of dynamic stress intensity factors.

Boundary element methods have, in recent years, proved very successful in solving static crack problems [3]. However, the application to dynamic crack problems is relatively new and the subject of current research. The so-called direct boundary integral equations have been applied to crack problems by many researchers, for example in [4] using the multi-region formulation, and more recently in [5] using the dual boundary element method. Other formulations can be found in [6–8].

An alternative formulation to the direct method is the indirect method which relates the displacement and stresses to fictitious source densities. Two indirect formulations known as the fictitious stress and the displacement discontinuity methods were developed in [9] for two-dimensional static problems. Recently, these formulations were extended to dynamic problems in [10]. In this paper, the displacement discontinuity method is presented in Laplace transform space. The equivalent stress method as described in [11] is extended to calculate the dynamic stress intensity factors $K_I(t)$ and $K_{II}(t)$ for an isolated crack in an infinite sheet. The influence of different elastic waves, particularly the surface waves, is analysed in detail. This method can be extended to determine stress intensity factors for three-dimensional crack problems.

2 The fundamental solutions for discontinuity displacement solution

In the Laplace space, the basic equations for the transformed variables are the same as in [10]. A Laplace transformed variable $f^*(p)$ is derived from the time-dependent variable $f(t)$

Received 18 May 1995; accepted for publication 1 October 1995

P. H. Wen[1], M. H. Aliabadi
Wessex Institute of Technology, Ashurst, Southampton, UK

D. P. Rooke
Structural Materials Centre, DRA, Farnborough, Hants, UK

[1] On leave from the Central-South University of Technology, Changsha, P.R. China

as follows:

$$f^*(p) = \int_0^\infty f(t) e^{-pt} dt.$$

For u_y^*, the mode-I displacement discontinuity, the boundary conditions on the x axis are

$$u_y^* = \begin{cases} u_I^* & -a \leqq x \leqq a \\ 0 & \text{otherwise} \end{cases}, \quad \sigma_{xy}^* = 0 \quad |x| < \infty; \tag{1}$$

and for u_x^*, the mode-II displacement discontinuity

$$u_x^* = \begin{cases} u_{II}^* & -a \leqq x \leqq a \\ 0 & \text{otherwise} \end{cases}, \quad \sigma_{yy}^* = 0 \quad |x| < \infty. \tag{2}$$

The fundamental solutions for the stress components σ_{yy}^* and σ_{xy}^* are given by

$$\begin{aligned} \sigma_{yy}^*(x,y,p) &= \frac{2u_I^*}{\pi}\left[\left(\mu + \lambda\left(\frac{\beta_1}{\beta_2}\right)^2\right)\frac{\partial \mathscr{K}^{(1)}}{\partial x} + \frac{2\mu}{\beta_2^2}\left(\frac{\partial^3 \mathscr{K}^{(1)}}{\partial x\,\partial y^2} - \frac{\partial^3 \mathscr{K}^{(2)}}{\partial x\,\partial y^2}\right)\right]_{x-a}^{x+a} - \frac{\beta_1^2 u_I^*}{\pi}(2\mu+\lambda)\int_{x-a}^{x+a} \mathscr{K}^{(1)}\,dx \\ &= f_I(x,y,p)\,u_I^* \end{aligned} \tag{3}$$

and

$$\begin{aligned} \sigma_{xy}^*(x,y,\tau) &= \frac{4\mu u_{II}^*}{\pi}\left[-\frac{1}{\beta_2^2}\frac{\partial^3 \mathscr{K}^{(1)}}{\partial x\,\partial y^2} + \left(\frac{\partial \mathscr{K}^{(2)}}{\partial x} - \frac{1}{\beta_2^2}\frac{\partial^3 \mathscr{K}^{(1)}}{\partial x^3}\right)\right]_{x-a}^{x+a} - \frac{\mu\beta_2^2 u_{II}^*}{\pi}\int_{x-a}^{x+a} \mathscr{K}^{(2)}\,dx \\ &= f_{II}(x,y,p)\,u_{II}^*; \end{aligned} \tag{4}$$

where

$$\mathscr{K}^{(1)} = \mathscr{K}_0(\beta_1\sqrt{x^2+y^2}), \quad \mathscr{K}^{(2)} = \mathscr{K}_0(\beta_2\sqrt{x^2+y^2}),$$

$\mathscr{K}_0(z)$ is a zero-order Bessel's function; $\beta_1 = p/c_1$, $\beta_2 = p/c_2$; c_1 and c_2 are the velocities of longitudinal and transverse waves respectively; p is the Laplace transform parameter; λ and μ are the Lamé elastic constants.

As only straight-line cracks in infinite bodies are considered here, the fundamental solution on the x axis $\sigma_{yy}^*(x,0,p)$ is the only one required, and, therefore, the boundary element formulation can be written [10] as

$$\sigma_{yy}^*(x,0,p) = f_I(x,0,p)\,u_I^*, \tag{5}$$

where

$$\begin{aligned} f_I(x,0,p) = {} & \frac{2G}{\pi(1+\nu)}\frac{a}{x^2-a^2} + \frac{1}{2}\sum_{k=0}^{\infty}\left\{\left[-\frac{\beta_2^2-2\beta_1^2}{\beta_1}A^*\left(\psi(k+1) - \ln\frac{z}{2} + \frac{1}{2k+1}\right)2(k+1)\right.\right. \\ & + 2\beta_1 A^*\left(\ln\frac{z}{2} - \frac{1}{2}\psi(k+1) - \frac{1}{2}\psi(k+2) - \frac{1}{2k+1}\right) \\ & + 6\beta_1 B^*\left(\psi(k+2) - \ln\frac{z}{2} + \frac{1}{2k+1}\right)\frac{1}{2(k+1)} \\ & + \frac{2\beta_1^2-\beta_2^2}{\beta_1}B^*\left(\ln\frac{z}{2} - \frac{1}{2}\psi(k+1) - \frac{1}{2}\psi(k+2) - \frac{1}{2k+1}\right) \\ & \left.\left. + 12\beta_1 B^*\left(\ln\frac{z}{2} - \frac{1}{2}\psi(k+2) - \frac{1}{2}\psi(k+3) - \frac{1}{2k+1}\right)\frac{1}{4(k+1)(k+2)}\right]\right. \\ & \left.\cdot\frac{z^{2k+1}}{2^{2k+1}k!(k+1)!(2k+1)}\right\}_{z=\beta_1(x+a)}^{z=\beta_1(x-a)} \\ & + \frac{1}{2}\sum_{k=0}^{\infty}\left\{\left[-6\frac{\beta_2^3}{\beta_1^2}B^*\left(\psi(k+2) - \ln\frac{z}{2} + \frac{1}{2k+1}\right)\frac{1}{2(k+1)}\right.\right. \end{aligned}$$

$$-2\frac{\beta_2^3}{\beta_1^2}B^*\left(\ln\frac{z}{2}-\frac{1}{2}\psi(k+1)-\frac{1}{2}\psi(k+2)-\frac{1}{2k+1}\right)$$

$$-12\frac{\beta_2^3}{\beta_1^2}B^*\left(\ln\frac{z}{2}-\frac{1}{2}\psi(k+2)-\frac{1}{2}\psi(k+3)-\frac{1}{2k+1}\right)\frac{1}{4(k+1)(k+2)}\Bigg]$$

$$\cdot\frac{z^{2k+1}}{2^{2k+1}k!(k+1)!(2k+1)}\Bigg\}_{z=\beta_2(x+a)}^{z=\beta_2(x-a)},$$

and

$$\sigma_{xy}^*(x,0,p)=f_{II}(x,0,p)\,u_{II}^*, \tag{6}$$

where

$$f_{II}(x,0,p)=\frac{2G}{\pi(1+\nu)}\frac{a}{x^2-a^2}-\frac{4\mu}{\pi}\frac{\beta_1^3}{\beta_2^2}\sum_{k=0}^{\infty}\left\{\left[3\left(\psi(k+1)-\ln\frac{z}{2}+\frac{1}{2k+1}\right)\frac{1}{2(k+1)}\right.\right.$$

$$+\left(\ln\frac{z}{2}-\frac{1}{2}\psi(k+1)-\frac{1}{2}\psi(k+2)-\frac{1}{2k+1}\right)$$

$$+6\left(\ln\frac{z}{2}-\frac{1}{2}\psi(k+2)-\frac{1}{2}\psi(k+3)-\frac{1}{2k+1}\right)$$

$$\left.\cdot\frac{1}{4(k+1)(k+2)}\right]\frac{z^{2k+1}}{2^{2k+1}k!(k+1)!(2k+1)}\Bigg\}_{z=\beta_1(x+a)}^{z=\beta_1(x-a)}$$

$$+\frac{\mu\beta_2}{\pi}\sum_{k=0}^{\infty}\left\{\left[\left(\psi(k+1)-\ln\frac{z}{2}+\frac{1}{2k+1}\right)2(k+1)+12\left(\psi(k+2)-\ln\frac{z}{2}+\frac{1}{2k+1}\right)\right.\right.$$

$$\cdot\frac{1}{2(k+1)}+4\left(\ln\frac{z}{2}-\frac{1}{2}\psi(k+1)-\frac{1}{2}\psi(k+2)-\frac{1}{2k+1}\right)$$

$$\left.+24\left(\ln\frac{z}{2}-\frac{1}{2}\psi(k+2)-\frac{1}{2}\psi(k+3)-\frac{1}{2k+1}\right)\frac{1}{4(k+1)(k+2)}\right]$$

$$\cdot\frac{z^{2k+1}}{2^{2k+1}k!(k+1)!(2k+1)}\Bigg\}_{z=\beta_2(x+a)}^{z=\beta_2(x-a)},$$

where

$$A^*=-\frac{2\lambda}{\pi}\frac{\beta_1}{\beta_2},\quad B^*=\frac{4\mu}{\pi}\frac{\beta_1^2}{\beta_2^2},$$

$$\psi(k)=\sum_{m=1}^{k-1}\frac{1}{m}-\tilde{\gamma},$$

$\tilde{\gamma}$ is the Euler constant ($\tilde{\gamma}=0.577$). It can be seen from the solutions in (5) and (6) that there are two parts. The first part is independent of the Laplace transform parameter p, since it is the solution for an elastostatic problem. The second term may be considered as the modification term in Laplace space, and is a function of the transform parameter p.

3
The calculation of dynamic stress intensity factor

Suppose that x_i is the nodal coordinate of constant element $i(i=1,2,\ldots,N)$, and a_i is the half-length of that element ($a_i=c/N$, where $2c$ is the length of the line crack). For a mode I problem, the influence of element j on element i can be determined from the solution in (3) when the stresses are put equal

to the boundary value $\sigma_0^*(p)$ in Laplace space

$$\sigma_{yy}^{*i} = \sum_{j=1}^{N} f_I(x_i - x_j, 0, p)\, u_I^{*j} = \sigma_0^{*i}(p), \tag{7}$$

where u_I^{*i} is the displacement discontinuity of element j in the y-direction. As $a_i = a_j$, then $f_I(x_i - x_j, 0, p) = f_I(x_j - x_i, 0, p)$, so that the coefficient matrix **C**, below, is symmetric. At a given sample point p_k, we have

$$\mathbf{C}\,\mathbf{U} = \mathbf{Y}, \tag{8}$$

where

$$\mathbf{U} = \{u_I^{*1}, u_I^{*2}, \ldots, u_I^{*N}\}^{\mathsf{T}} \quad \text{and} \quad \mathbf{Y} = \{\sigma_0^{*1}, \sigma_0^{*2}, \ldots, \sigma_0^{*N}\}^{\mathsf{T}}. \tag{9}$$

If there is only a normal load σ_0^* on the crack surface, the stress intensity factor K_{II}^* is zero. In a similar way, the displacement discontinuity u_x^{*j} for mode II can be determined. After the displacement discontinuties are determined on each element, the equivalent normal and transverse stresses $\tilde{\sigma}_n^*$ and $\tilde{\sigma}_s^*$ on all of the elements can be determined [11] by

$$\tilde{\sigma}_n^{*i} = \sum_{j=1}^{N} \frac{2Ga_j\, u_y^{*j}}{\pi(1-\nu)[(x_j - x_i)^2 - a_j^2]} = \sum_{j=1}^{N} \alpha_{ij}\, u_I^{*j},$$

and

$$\tilde{\sigma}_s^{*i} = \sum_{j=1}^{N} \frac{2Ga_j\, u_x^{*j}}{\pi(1-\nu)[(x_j - x_i)^2 - a_j^2]} = \sum_{j=1}^{N} \alpha_{ij}\, u_{II}^{*j}. \tag{10}$$

Then, the stress intensity factor at the right-hand tip of a crack in Laplace space is given by

$$K_I^*(p_k) = \sum_{i=1}^{N}\sum_{j=1}^{N} \alpha_{ij} F_i\, u_y^{*j} \sqrt{\pi c} = \sum_{j=1}^{N} \lambda_j\, u_I^{*j} \sqrt{\pi c}, \tag{11}$$

where

$$F_i = \frac{1}{\pi c} \int_{x_i - a_i}^{x_i + a_i} \sqrt{\frac{c+x}{c-x}}\, dx = \frac{1}{\pi}\left[\arcsin\left(\frac{x}{c}\right) - \sqrt{1 - \left(\frac{x}{c}\right)^2} \right]_{x_i - a_i}^{x_i + a_i},$$

and

$$\lambda_j = \sum_{i=1}^{N} \alpha_{ij} F_i.$$

Once the stress intensity factors $K_I^*(p_k)$ are determined, the stress intensity factor in the time domain $K_I(t)$ can be obtained from Durbin's inversion formula [12], as

$$K_I(t) = 2\frac{e^{\theta t}}{T}\left\langle -\frac{1}{2}\Re\left[K_I^*(p_0)\right] + \sum_{k=0}^{M_p}\left\{\Re\left[K_I^*(p_k)\cos\frac{2k\pi t}{T}\right] - \Im\left[K_I^*(p_k)\sin\frac{2k\pi t}{T}\right]\right\}\right\rangle, \tag{12}$$

where $\Re[\,]$ and $\Im[\,]$ denote the real and imaginary parts, respectively. In this work, the Laplace sample points p_k were determined by $p_k = (\theta T + i2k\pi)/T$, $k = 0, 1, \ldots, M_p$, where $\theta T = 5$ and $T = 20c/c_1$; M_p is the number of sample points. The calculation method for mode-II stress intensity factors $K_{II}(t)$ is the same as that for mode *I*.

4
Numerical examples

4.1
Uniform load on the crack surface

An isolated crack of length $2c$ in an infinite sheet is subjected to a uniform opening load $\sigma_0 H(t)$ or a uniform sliding load $\tau_0 H(t)$, where $H(t)$ is the Heaviside function. Poisson's ratio ν is taken as 0.25. The number of elements $N = 80$ and the number of sample points in Laplace space $M_p = 150$. In this case, the velocities of transverse and surface waves, c_2 and c_R, are 0.5774 c_1 and 0.5309 c_1, respectively.

In Fig. 1 the ratio of the dynamic stress intensity factor to the static (long time) value is plotted; it can be seen that there are many kinks for both of the dynamic stress intensity factors, K_I and K_{II}. The positions of the kinks are determined by the times of arrival at the crack tip of the different elastic waves. The results in [13] are also shown for comparison.

For the opening-mode stress intensity factor K_I, the coordinate of the first kink A is given by $\bar{t} = \bar{t}_R = c_1/c_R = 1.884$, where $\bar{t}$ is the non-dimensional time $c_1 t/(2c)$; $\bar{t}_R$ is the time required for stress surface waves to travel from one crack tip to the other tip. It is clear that the first kink is thus caused by the arrival of this surface wave. The second one B is due to the surface wave starting from one tip (at $t = 0$) and travelling to the other and back; it occurs at $\bar{t} = 2\bar{t}_R = 3.76$. Further kinks of decreasing sharpness (for example C) are observed at periods of $\bar{t}_R$, as the surface waves oscillate between the tips. Thus surface waves account for all the kinks in K_I. For $\bar{t} > 4$, the value of K_I tends to the static value.

In contrast, kinks in K_{II} are caused by both surface and dilatation waves. The position of the first kink D at $\bar{t} = \bar{t}_1 = 1$, is caused by the dilatation wave leaving one tip at $t = 0$ and travelling to the other at velocity c_1. After this point, the curve of K_{II} is smooth until $\bar{t} = \bar{t}_R$, the time for the surface wave to travel from tip to tip, causing a second kink. A second kink due to dilatation waves occurs at $\bar{t} = 2\bar{t}_1 = 2$; it is difficult to detect because of its closeness to the kink at $\bar{t}_R$. Further periodic kinks for K_{II} are caused by further reflections of both dilatation waves and surface waves. Thus it can be seen that the stress intensity factor K_{II} is sensitive to both dilatation and surface waves. The influence of these oscillating elastic waes declines very rapidly; for $\bar{t} > 3$, the dynamic stress intensity factor is virtually the same as the static value $\tau_0\sqrt{\pi c}$.

The influence of these ocillating elastic waves on the stress intensity factors can be seen even more clearly in the following examples.

4.2
Interference between two cracks

There are two collinear cracks AB and CD shown in Fig. 2 with a uniform opening load $\sigma_0 H(t)$ acting on the crack faces of AB. The length of each of the two cracks is $2c$, and the distance between crack tips B and C is c. The parameters ν, M_p and the number of elements N are the same as in Example 1. The stress intensity factors at these four crack tips are shown in Fig. 2. When $\bar{t} < 3.768 (= 2\bar{t}_R)$, there

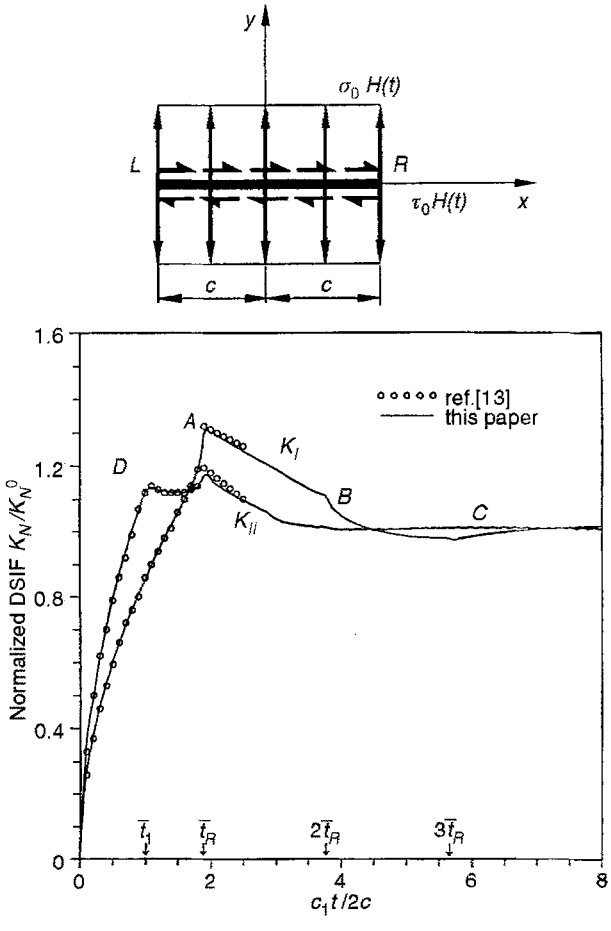

Fig. 1. Dynamic K_I and K_{II} for an isolated loaded crack

is no difference between K_I^A and K_I^B. The other two K_I^C and K_I^D are zero before the dilatation wave starting from crack tip B arrives at the points C and D (at $\bar{t} = 0.5$ and $\bar{t} = 1.5$, respectively). After this wave arrives, the calculated stress intensity factors K_I^C and K_I^D are less than zero, which means the crack closure has occurred. There are three kinks for curve K_I^D at *a*, *b*, and *c* (shown in Fig. 2). The first kink *a* occurs at $\bar{t} = 0.866 + 1.884 = 2.75$ and is caused by a stress wave starting from crack tip B travelling through the body from B to C at the speed c_2 of transverse waves, and then along the crack CD at the surface wave speed (c_R). The second kink *b* at $\bar{t} = 1.884 + 0.866 + 1.884 = 4.634$ is caused by the arrival of a stress wave starting from crack tip A travelling to tip B at the speed of surface waves, and from B to C at the speed of shear waves and then to D at the surface wave velocity. The last kink *c* at $\bar{t} = 3.768 + 0.866 + 1.884 = 6.518$ is caused by a stress wave starting from point B travelling to point A and then being reflected to point D along the same path as the wave causing kink *b*. For the stress intensity factor K_I^C, there is only one weak kink at *c'* caused by a stress wave starting from point D at the time $\bar{t} = 4.634$ (kink *b* in K_I^D) and travelling at the speed of surface waves to tip C.

4.3
Point forces at the mid-point of the crack

Two pairs of concentrated forces $\mathbf{P}H(t)$ and $\mathbf{Q}H(t)$ act at the mid-point of a crack in the normal and tangential directions, respectively, Fig. 3. Poisson's ratio ν is taken as 0.25, $N = 100$ and $M_p = 200$. The normalized stress intensity factors $K_I(t)/K_I^0$ and $K_{II}(t)/K_{II}^0$ are also shown in Fig. 3, were $K_I^0 = \mathbf{P}/\sqrt{\pi c}$ and $K_{II}^0 = \mathbf{Q}/\sqrt{\pi c}$. The influence on the dynamic stress intensity factors of the elastic waves oscillating between the tips can be clearly seen. Kinks are caused by both surface waves and dilatation waves. As in the first example, the stress intensity factor $K_{II}(t)$ is more sensitive than K_I, and the effects for both decline very rapidly.

For the mode I stress intensity factor, there is a small change when the dilatation waves arrive simultaneously at both crack tips from the central point at $\bar{t} = \bar{t}_1/2 = 0.5$. It should be noted that $K_I(t) < 0$, which means that crack closure would occur in practice (not considered here). When the

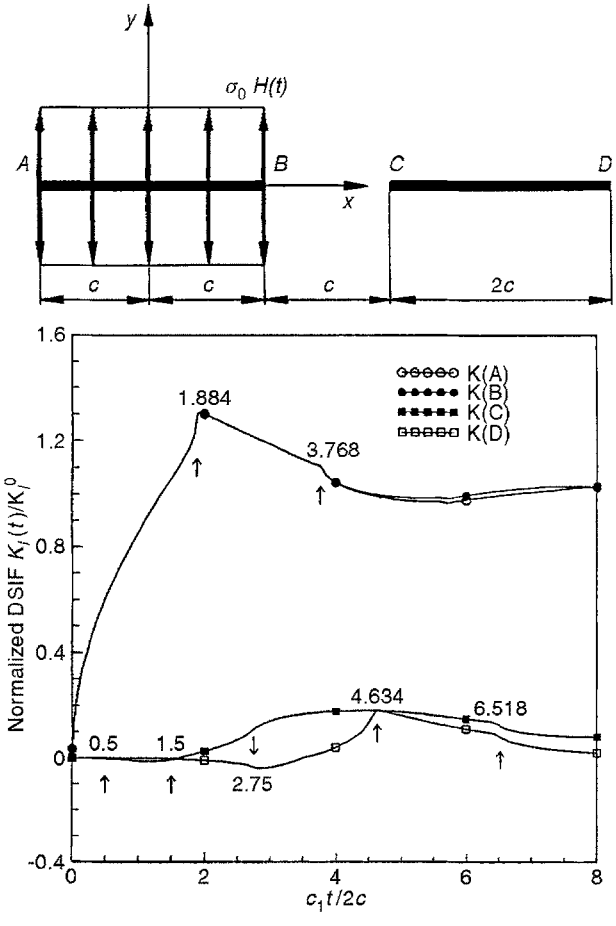

Fig. 2. The interference between two cracks

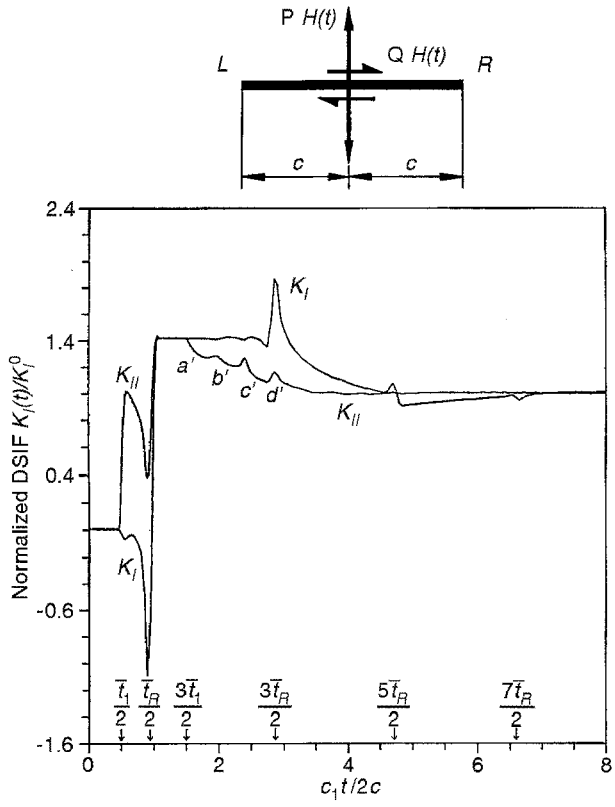

Fig. 3. Dynamic K_I and K_{II} for an isolated loaded crack loaded by concentrated force

first surface wave arrives at the tip, at $\bar{t} = \bar{t}_R/2$, the K_I is singular and discontinuous. That is

$$\lim_{\varepsilon \to 0} \left[K_I \left(\bar{t} = \frac{\bar{t}_R}{2} - \varepsilon \right) \right] = -\infty,$$

$$\lim_{\varepsilon \to 0} \left[K_I \left(\bar{t} = \frac{\bar{t}_R}{2} + \varepsilon \right) \right] = \sqrt{2} K_I^0. \tag{13}$$

These limits agree with Freund's solution [1] for a semi-infinite crack. The second major kink is due to a surface wave starting from the mid-point at $\bar{t} = 0$, travelling to one tip and being reflected to the other, arriving at $\bar{t} = 3\bar{t}_R/2$. The second kink is weaker than the first one. Further weaker kinks occur at $\bar{t} = 5\bar{t}_R/2$ and $\bar{t} = 7\bar{t}_R/2$ after which K_I is constant at the static value.

For the mode-II stress intensity factor, the first jump occurs at $\bar{t}_1/2$ and is due to the arrival of the first dilatation wave from the mid-point. The second jump at $\bar{t}_R/2$ is similar to that of K_I and is caused by arrival of the first surface wave. The stress intensity factor $K_{II}(t)$ displays a similar singularity character to that of $K_I(t)$ at $\bar{t}_R/2$. As in mode I, the stress intensity factor $K_{II}(t)$ undergoes a discontinuous jump immediately after the first surface wave arrives. It remains constant until the reflected dilatation wave arrives at $3\bar{t}_1/2$ (kink a'), and then decreases rapidly. As with K_I, there is a further kink d' at $3\bar{t}_R/2$ due to the reflected surface wave, after which K_{II} rapidly tends to the static value.

In general, there are many kinks generated by the different waves. They are detailed in Table 1, where the arrival times are shown for different combinations of stress waves starting from the central point, travelling to the left-hand crack tip, and then reflecting from this tip to the right-hand crack tip. The first line denotes the speed of the initial elastic wave, the second line is the reflected wave speed, and the last line is the arrival time at the tip after one reflection. Some of these kinks (a', b', c' and d') can be seen in Fig. 3.

The normalized opening displacements on the crack faces $u_y E/P$ are shown in Fig. 4. When $\bar{t}$ is less than 0.5, there is no displacement of the crack surface near the crack tip ($u_y = 0$). The results show negative displacements close to the tip for $0.5 < \bar{t} < 0.943$ due to longitudinal waves. At $\bar{t} = 0.943$ the surface wave front arrives, and the crack tip starts to open and remains open. Thus crack

Table 1. The timetable of stress-wave arrivals

Initial speed	c_1			c_2			c_R		
Reflected speed	c_1	c_2	c_R	c_1	c_2	c_R	c_1	c_2	c_R
Arrival time $\bar{t}$	1.5 (a')	2.23	2.39 (c')	1.87	2.60	2.75	1.94 (b')	2.68	2.83 (d')

closure would occur in practice for a period of time. The positive displacements near the tip are independent of time until the reflected dilatation wave arrives at $\bar{t} = 1.5$. The disturbances in the displacement caused by the reflected wave are very small.

4.4
Crack face loads continuously varying with time

Let there be a normal load $\sigma_0 f_n(t)$ acting on the crack surface, where

$$f_n(t) = \left(\frac{c_2 t}{c}\right)^n e^{-c_2 t/c}, \quad n = 0, 1, 2, 3, t \geqq 0.$$

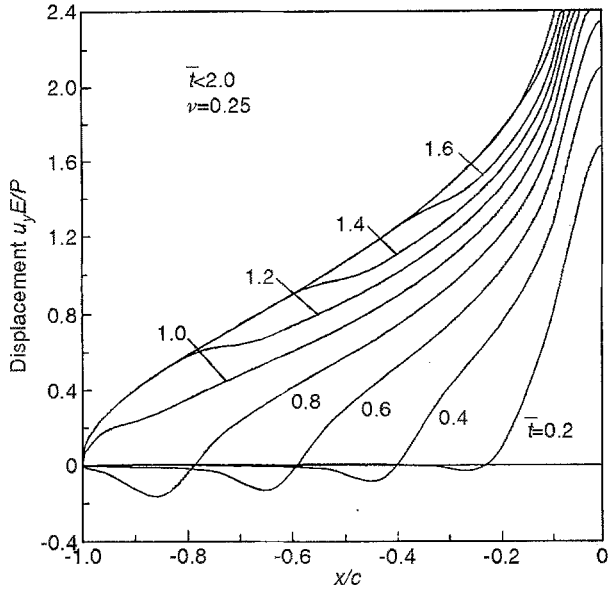

Fig. 4. The displacement for concentrated forces

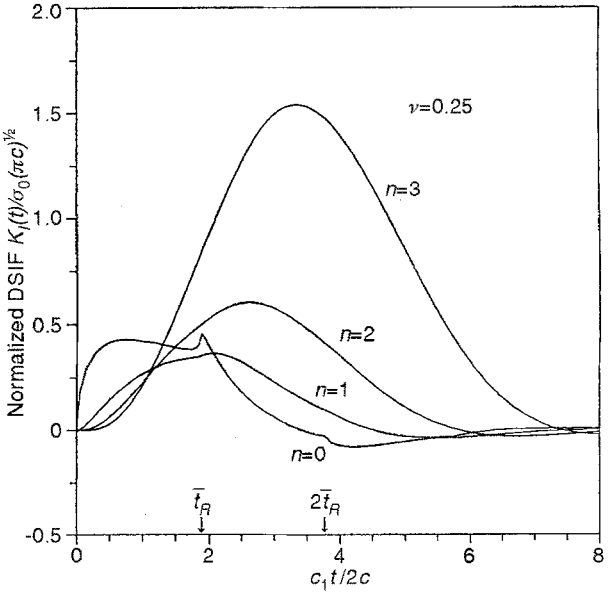

Fig. 5. Dynamic K_I for different loads

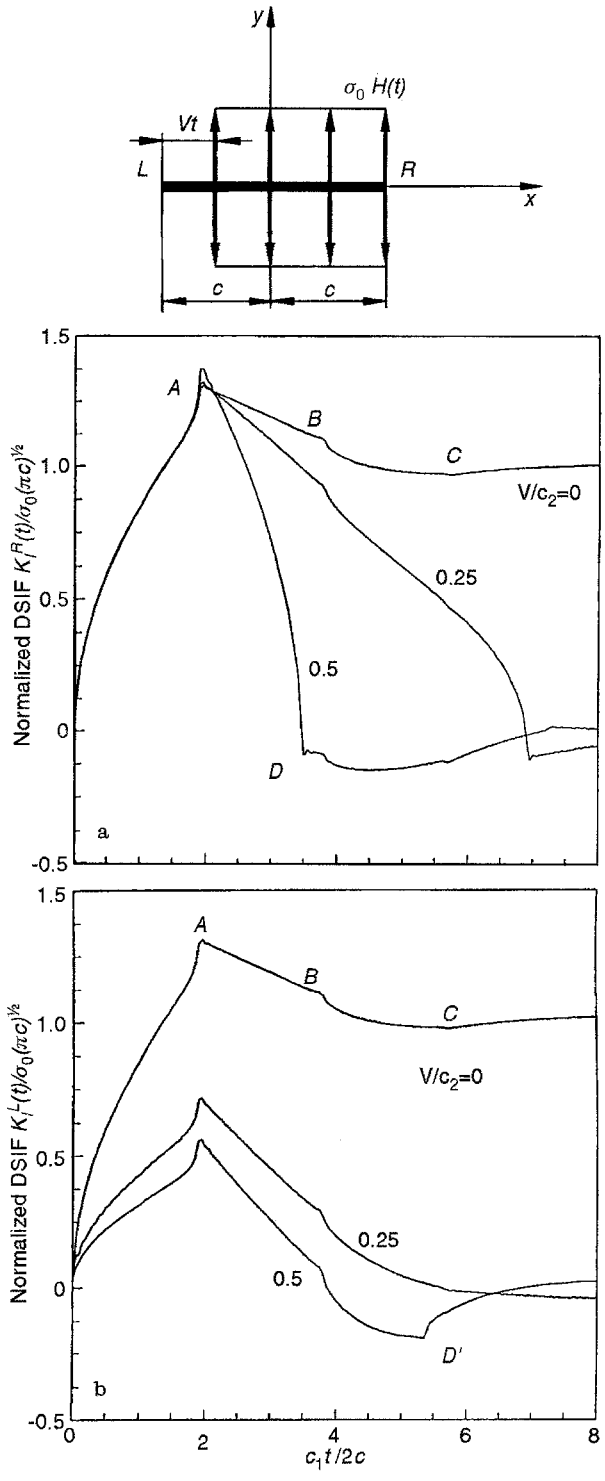

Fig. 6. Dynamic K_I for a moving load on the crack surface

For Poisson's ratio $v = 0.25$, $N = 80$ and $M_p = 150$, the dynamic stress intensity factors, normalized with respect to $\sigma_0\sqrt{\pi c}$, are shown in Fig. 5. The influence of surface waves on these stress intensity factors can be seen clearly in the case of $n = 0$. However, when $n = 1, 2$ or 3, the influence is much less and the curves of the variation of the stress intensity factor with time are virtually smooth.

4.5
Moving load on the crack faces

Consider a moving load on the crack surface: a uniform opening load moves from the left-hand tip (L) to the right-hand tip (R) with a speed of V, Fig. 6. The boundary condition on the crack surface

can be written as

$$\sigma(x,t) = \sigma_0\left[H(t) - H\left(t - \frac{x+c}{V}\right)\right];$$

where $H(t)$ is the Heaviside function. For Poisson's ratio $v = 0.25$, $N = 100$ and $M_p = 150$, the stress intensity factors K_I^R and K_I^L are shown in Fig. 6. There are many jumps and kinks both for K_I^R (right) and K_I^L (left) due to surface waves. From Fig. 6(a), it can be seen that the maximum value (at A) of the stress intensity factor K_I^R increases slightly with speed V. For all speeds, the kink points A, B and C are caused by surface waves, the same waves as when $V = 0$. For $V/c_2 = 0.5$ the kink D for K_I^R coincides with the arrival of the edge of the moving load at tip R. The surface wave caused by the arrival of the moving load at R arrives at the crack tip L a time $\bar{t}_R$ later; this is the kink D' in the stress intensity factor K_I^L shown in Fig. 6(b). All of the other kink points for these stress intensity factor curves can be analysed in a similar way.

5 Conclusions

The procedure for determining dynamic stress intensity factors by a displacement discontinuity method is outlined in this paper. By the use of Laplace transforms, the basic solutions for a constant displacement discontinuity element were deduced. The stress intensity factors in Laplace space $K_N^*(p)$ were calculated by an equivalent stress method. The dynamic stress intensity factors $K_N(t)$ were determined by the Durbin inversion method. Numerous numerical examples are given in this paper, and the influence of different elastic waves, particularly the surface waves, on dynamic stress intensity factors is highlighted.

References

1. **Freund, L. B.:** Dynamic fracture mechanics. Cambridge: Cambridge University Press 1990
2. **Chen, Y. M.:** Numerical computation of dynamic stress intensity factors by a Lagrangian finite-difference method (the HEMP CODE). Eng. Fract. Mech. 7 (1975) 653–660
3. **Aliabadi, M. H.; Rooke, D. P.:** Numerical fracture mechanics. Southampton: Computational Mechanics Publications 1991
4. **Dominguez, J.; Gallego, F.:** Time domain boundary element method for dynamic stress intensity factor computations. Int. J. Num. Meth. Eng. 33 (1992) 635–647
5. **Fedelinski, P.; Aliabadi, M. H.; Rooke, D. P.:** Dynamic stress intensity factors in mixed-mode: time domain formulation. In: Brebbia, C.A. Boundary Element Method XVI, Southampton: Computational Mechanics Publication pp. 513–520. 1994
6. **Zhang, Ch.; Achenbach, J. D.:** Time-domain boundary element analysis of dynamic near-tip fields for impact loaded collinear cracks. Eng. Fract. Mech. 32 (1989) 899–900
7. **Zhang, Ch.; Gross, D.:** A non-hypersingular time-domain BIEM for 3D transient elastodynamic crack analysis. Int. J. Num. Meth. Eng. 36 (1993) 2997–3017
8. **Nishimura, N.; Guo, Q. C.; Kobayashi, S.:** Boundary integral equation methods in elastodynamic crack problems., In: Brebbia, C.A.; Wendland, W.L.; Kuhn, G. Proc. Boundary Element IX, vol 2, Stress Analysis Applications, Springer Computational Mechanics Publications pp. 279–291 (1987)
9. **Crouch, S. L.; Starfield, A. M.:** Boundary element method in solid mechanics. London: Allen and Unwin 1983
10. **Wen, P. H.; Aliabadi, M. H.; Rooke, D. P.:** A ficitious stress and displacement discontinuity method for dynamic crack problems. In: Brebbia, C.A. (ed.) Proc. Boundary Element Method XVI, Southampton: Computational Mechanics Publications 1994
11. **Wen, P. H.; Wang, Y.:** The calculation of SIF considering the effects of arc crack surfaces contact and friction under uniaxial tension and pressure. Eng. Fract. Mech. 39 (1991) 651–660
12. **Durbin, F.:** Numerical inversion of Laplace transforms: an efficient improvement to Dubner and Abate's method. The Computer J. 17 (1974) 371–376
13. **Stephen, A. T.; Lu, T. H.:** Transient stress intensity factors for a finite crack in an elastic solid caused by a dilatational wave. Int. J. Solids Struct. 7 (1971) 731–750